

# High-Load Gemcitabine Inorganic–Organic Hybrid Nanoparticles as an Image-Guided Tumor-Selective Drug-Delivery System to Treat Pancreatic Cancer

Myrto Ischyropoulou, Kristina Sabljo, Leonie Schneider, Christof M. Niemeyer, Joanna Napp,\* Claus Feldmann,\* and Frauke Alves\*

Pancreatic ductal adenocarcinoma (PDAC) has a devastating prognosis without effective treatment options. Thus, there is an urgent need for more effective and safe therapies. Here, inorganic–organic hybrid nanoparticles (GMP-IOH-NPs) are presented as a novel drug-delivery system for the selective delivery of extraordinarily high concentrations of gemcitabine monophosphate (GMP), not only to the primary tumor but also to metastatic sites. GMP-IOH-NPs have a composition of  $[\text{ZrO}]^{2+}[\text{GMP}]^{2-}$  with GMP as drug anion (76% of total IOH-NP mass). Multiscale fluorescence imaging confirms an efficient uptake in tumor cells, independent of the activity of the human-equilibrative-nucleoside transporter (hENT1), being responsible for gemcitabine (GEM) transport into cells and a key factor for GEM resistance. Delivering already phosphorylated GMP via GMP-IOH-NPs into tumor cells also allows the cellular resistance induced by the downregulation of deoxycytidine kinase to be overcome. GMP-IOH-NPs show high accumulation in tumor lesions and only minor liver trapping when given intraperitoneally. GMP-IOH-NPs result in a higher antitumor efficacy compared to free GEM, which is further enhanced applying cetuximab-functionalized GMP-CTX-IOH-NPs. By maximizing the therapeutic benefits with high drug load, tumor-specific delivery, minimizing undesired side effects, overcoming mechanisms of chemoresistance, and preventing systemic GEM inactivation, GMP-IOH-NPs are anticipated to have a high chance to significantly improve current PDAC-patient outcome.

## 1. Introduction

Pancreatic ductal adenocarcinoma (PDAC) is one of the most lethal human cancers,<sup>[1]</sup> ranking the fourth leading cause of cancer-related deaths in the western world. Such dismal prognosis can be traced back to both its late detection—often due to a lack of symptoms in early stages—and to treatment failure—especially in advanced tumors not eligible for complete surgical resection.<sup>[2]</sup> Therefore, effective therapeutic strategies not only against the primary tumor but also its metastasis (most often in liver, peritoneum and lung) are urgently needed for patients with late stage PDAC.<sup>[3]</sup> Currently, systemic chemotherapy represents the standard treatment either in neo-adjuvant, adjuvant and palliative settings, regrettably resulting in only modest improvement of survival.<sup>[4]</sup> Since the late 1990s, the nucleoside analogue gemcitabine (GEM, 2',2'-difluoro-2'-deoxycytidine) has been the first-line drug for advanced PDAC. GEM is preferentially applied in combination therapies (e.g., with nab-paclitaxel, cisplatin, capecitabine, erlotinib), selected

M. Ischyropoulou, J. Napp, F. Alves  
Department of Diagnostic and Interventional Radiology  
University Medical Center Goettingen (UMG)  
Robert-Koch-Strasse 40, 37075 Goettingen, Germany  
E-mail: napp@mpinat.mpg.de; falves@gwdg.de

M. Ischyropoulou, J. Napp, F. Alves  
Max Planck Institute for Multidisciplinary Sciences (MPI-NAT)  
Hermann-Rein-Strasse 3, 37075 Goettingen, Germany

K. Sabljo, C. Feldmann  
Institute of Inorganic Chemistry  
Karlsruhe Institute of Technology (KIT)  
Engesserstrasse 15, 76131 Karlsruhe, Germany  
E-mail: claus.feldmann@kit.edu

L. Schneider, C. M. Niemeyer  
Institute for Biological Interfaces 1  
Karlsruhe Institute of Technology (KIT)  
Hermann-von-Helmholtz Platz 1, 76344 Eggenstein-Leopoldshafen,  
Germany

F. Alves  
Department of Haematology and Medical Oncology  
University Medical Center Goettingen (UMG)  
Robert-Koch-Strasse 40, 37075 Goettingen, Germany

 The ORCID identification number(s) for the author(s) of this article can be found under <https://doi.org/10.1002/adma.202305151>

© 2023 The Authors. Advanced Materials published by Wiley-VCH GmbH. This is an open access article under the terms of the Creative Commons Attribution-NonCommercial-NoDerivs License, which permits use and distribution in any medium, provided the original work is properly cited, the use is non-commercial and no modifications or adaptations are made.

DOI: 10.1002/adma.202305151

based on the tumor stage and the general performance status. Although other regimens are available (e.g., FOLFIRINOX: combination of 5-fluorouracil, leucovorin, irinotecan, oxaliplatin), GEM is still a key-compound for PDAC treatment. Yet, its clinical efficacy is severely limited by its short half-life and rapid elimination from the body by conversion into inactive 2',2'-difluorodeoxyuridine by the enzyme cytidine deaminase (CDA) abundant in plasma and liver.<sup>[5]</sup> Therefore, usually high GEM doses need to be repeatedly given to patients, which not only lead to systemic toxicity (e.g., hepato-/nephrotoxicity) but also promotes chemoresistance.<sup>[6]</sup>

Since GEM is a hydrophilic moiety, it needs to be transported into the tumor cells via different nucleoside transporters, e.g. the human equilibrative nucleoside transporter (hENT1),<sup>[7]</sup> whose biological activity is considered to be a prerequisite for the efficacy of GEM. After entering the cell, free GEM undergoes intracellular conversion by a series of phosphorylation steps mediated by specific enzymes. First of all, deoxycytidine kinase (dCK) phosphorylates GEM to the nucleotide gemcitabine monophosphate (GMP), and subsequently pyrimidine nucleoside monophosphate kinase (NMPK) to gemcitabine diphosphate. The latter is finally activated by phosphorylation to gemcitabine triphosphate (GTP) by the nucleoside diphosphate kinase (NDPK) that competes with deoxycytidine triphosphate (dCTP) for the incorporation into DNA, leading to an inhibition of DNA synthesis.<sup>[8]</sup>

The most fundamental mechanisms of GEM chemoresistance are: i) downregulation of the nucleoside transporters, as their absence prevents GEM from entering cells, ii) decrease in expression of dCK being responsible for the first step of the GEM phosphorylation after cellular uptake,<sup>[9]</sup> and iii) enhanced GEM deactivation, causing GEM degradation and excretion, controlled by the enzyme cytidine deaminase, which is often upregulated in chemoresistant patients.<sup>[10]</sup> Another factor generally affecting the efficacy of chemotherapeutic drugs is the peculiar tumor microenvironment in PDAC with a highly dense, desmoplastic stroma. To circumvent the resistance to GEM derived from the physical and molecular barriers in PDAC, nanocarrier-based approaches (e.g., GEM-loaded solid-lipid nanocarriers, GEM embedded in (bio)polymer matrices or liposomes)<sup>[11]</sup> and various modifications of GEM (e.g., as prodrug)<sup>[12]</sup> have been suggested but yet suffer from insufficient drug load (<10% of total nanocarrier mass), multistep synthesis, complex nanocarrier composition and structure, and/or insufficient drug transport, delivery and efficacy. A nanocarrier-based transport of GMP, however, could not only be an option to bypass the hENT1 transporter, but also the initial step of GEM phosphorylation as the rate-limiting step to activate gemcitabine.<sup>[7]</sup> Both strategies have high potential to circumvent GEM resistance as already suggested for GEM-loaded liposomes, microemulsion-made calcium phosphate nanocarriers, or GMP-filled metal-organic framework (MOF)-type particles.<sup>[13]</sup> However, these nanocarriers exhibit complex, multicomponent compositions with only <1% to 10% of GEM/GMP and particle sizes partly up to 100  $\mu\text{m}$ .

Numerous pathways were described for the internalization of nanocarrier-based therapeutics into cells. After uptake, these pathways merge into early endosomes before undergoing sorting, where material may also be sent back to the surface via

recycling endosomes, traffic to late endosomes and lysosomes or escape from endocytic vesicles to the cytosol. Understanding the complex mechanisms and pathways, which can be different for different cell types, as well as for different nanocarriers, is a currently emerging issue.<sup>[14]</sup> Metabolic characteristics of cancer cells such as pH or increased glucose consumption can be used to direct nanocarriers to the tumor tissue. In this regard, glucose-coated nanocarriers were often reported to show a faster cancer-cell uptake.<sup>[15]</sup> To increase the tumor-specific uptake, moreover, many nanocarriers were equipped with specific ligands. Among them, the (human) epithelial growth factor receptor 1 ((h)EGFR1)—overexpressed in 70% of PDAC cases—has been successfully targeted with monoclonal antibodies (e.g., cetuximab, panitumumab), immunotoxins, ligand-binding cytotoxic agents, or small-molecule tyrosine-kinase inhibitors (e.g., erlotinib, gefitinib).<sup>[16]</sup> Beside cell uptake, detailed understanding of biodistribution, localization at target sites, accumulation and mechanisms for heterogeneous distribution in healthy organs and tissues are key to the successful transition of nanocarriers from basic research via preclinical development into clinical application. To this concern, fluorescence imaging (FI) has become a powerful tool for non-invasive imaging in preclinical setups, as well as with high spatial and temporal resolution to assess the nanocarrier distribution in tissue on a (sub-)cellular scale.<sup>[17]</sup>

Aiming at an efficient delivery of GEM to PDAC tumors, preferentially circumventing chemoresistance, we suggest inorganic–organic hybrid nanoparticles (IOH-NPs) as a novel drug-delivery system for selective delivery of extraordinarily high concentrations of already phosphorylated gemcitabine monophosphate (GMP) to the primary tumor and metastatic sites, followed by uptake into tumor cells, most likely via one of the endocytic pathways but independent of the activity of hENT1. Due to fluorescence labeling, the GMP-loaded IOH-NPs (GMP-IOH-NPs) are enabled for in vivo and ex vivo monitoring. Moreover, “naked” GMP-IOH-NPs are compared with glucose-coated (GMP-GLU-IOH-NPs) and cetuximab-functionalized (GMP-CTX-IOH-NPs) in regard of an efficient, selective accumulation at tumor sites and lesions. IOH-NP accumulation, tumor targeting, cytostatic efficacy, chemoresistance, and side effects are addressed to understand and to maximize the therapeutic benefits applying GMP-IOH-NPs.

## 2. Inorganic–Organic Hybrid Nanoparticles

### 2.1. Material Concept and Synthesis

Inorganic–organic hybrid nanoparticles (IOH-NPs) are characterized by a saline composition with an inorganic cation and a drug anion, which is functionalized by phosphate, sulfonate, or carboxylate groups.<sup>[18]</sup> Specifically, the concept of IOH-NPs comprises a simple synthesis in water, an extraordinarily high drug load (>60% of total nanoparticle mass), an uncomplex composition and structure of the nanocarriers, and a high adaptability of the IOH-NPs to use various drugs. Previous studies with antibiotic or anti-inflammatory drugs have already pointed to the feasibility of the material concept.<sup>[19]</sup> Here, gemcitabine monophosphate (GMP) is used as chemotherapeutic anion for the first time.

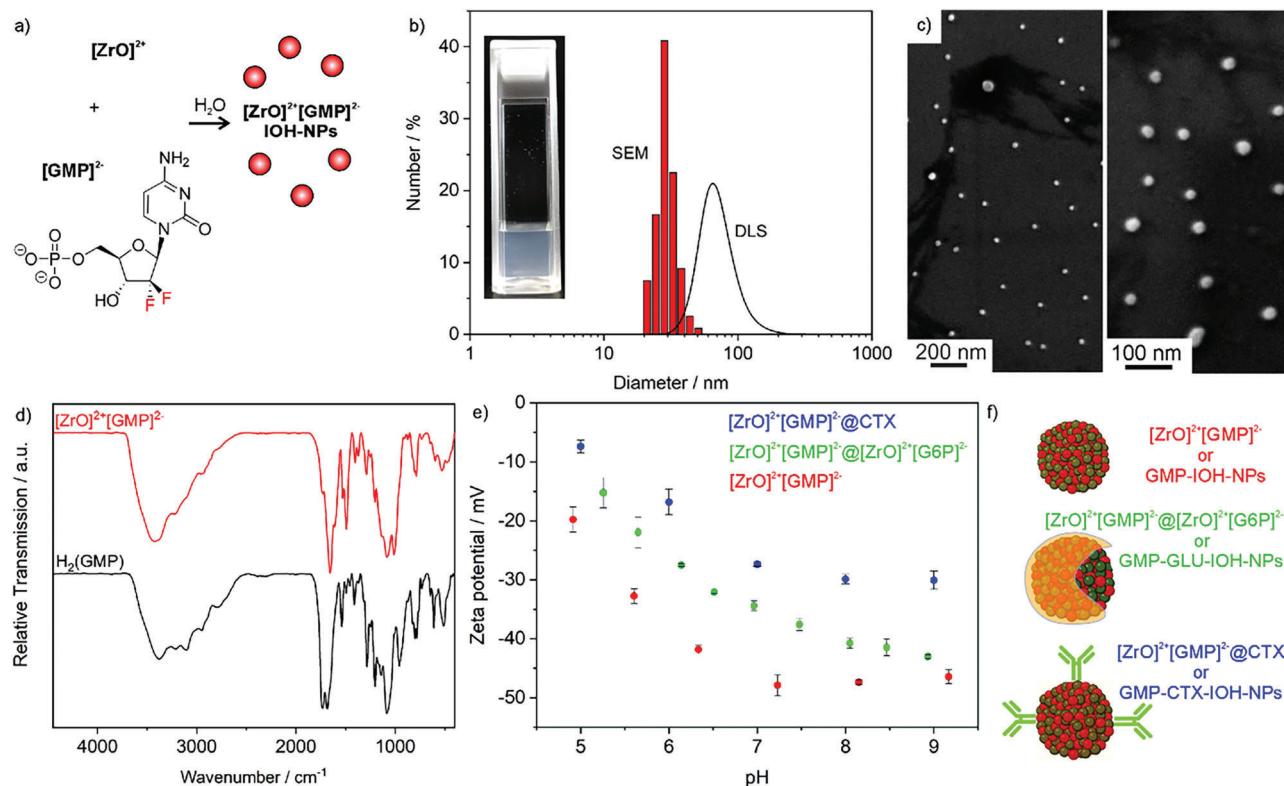


**Figure 1.** Synthesis and characterization of  $[\text{ZrO}]^{2+}[\text{GMP}]^{2-}$  IOH-NPs: a) Scheme illustrating the aqueous synthesis, b) particle size distribution according to DLS and SEM with photo of aqueous suspension, c) SEM images at different levels of magnification, d) FT-IR spectra (with  $\text{H}_2(\text{GMP})$  as a reference), e) zeta potential, including surface-functionalized  $[\text{ZrO}]^{2+}[\text{GMP}]^{2-} @ [\text{ZrO}]^{2+}[\text{G6P}]^{2-}$  and  $[\text{ZrO}]^{2+}[\text{GMP}]^{2-} @ \text{CTX}$  IOH-NPs (G6P: glucose-6-phosphate; CTX: cetuximab), and f) scheme of IOH-NPs with designation used for in vitro/in vivo studies. For further characterization see Figures S1–S7, Supporting Information.

Zirconyl ( $[\text{ZrO}]^{2+}$ ) is used as inorganic cation to make the drug insoluble in water and to obtain IOH-NPs with a saline composition  $[\text{ZrO}]^{2+}[\text{GMP}]^{2-}$  (Figure 1).

In detail,  $[\text{ZrO}]^{2+}[\text{GMP}]^{2-}$  IOH-NPs were synthesized by injection of aqueous  $\text{ZrOCl}_2 \cdot 8\text{H}_2\text{O}$  into an aqueous solution of  $\text{H}_2(\text{GMP})$  (Figure 1a), which, after purification (see Supporting Information), results in colloidal highly stable suspensions ( $5 \text{ mg mL}^{-1}$ ) that do not show any sedimentation over several weeks (Figure 1b). Particle size, size distribution and zeta-potential analysis were examined by dynamic light scattering (DLS) and scanning electron microscopy (SEM). Accordingly, a hydrodynamic diameter of  $69 \pm 16 \text{ nm}$  (DLS) and a diameter of  $29 \pm 4 \text{ nm}$  (SEM) were obtained with negative surface charging ( $-35 \pm 6 \text{ mV}$ ) (Figure 1b,c,e), which is also causative for the colloidal stability. The chemical composition of the  $[\text{ZrO}]^{2+}[\text{GMP}]^{2-}$  IOH-NPs was validated by different methods, including X-ray diffraction (XRD), energy-dispersive electron spectroscopy (EDXS), Fourier-transform infrared (FT-IR) spectroscopy, elemental analysis (EA, C/H/N/S analysis), and total organics combustion/thermogravimetry (TG) (Figure 1d; Figures S1–S6, Supporting Information). Whereas the presence of zirconium and GMP were qualitatively confirmed by EDXS and FT-IR, the  $[\text{ZrO}]^{2+} : [\text{GMP}]^{2-}$  ratio and the overall composition were quantified by EA and TG. In sum, the composition  $[\text{ZrO}]^{2+}[\text{GMP}]^{2-}$  with a GMP-load of 76% of the total IOH-

NP mass (24% due to  $[\text{ZrO}]^{2+}$  as inorganic cation) was confirmed. Here, it should be noticed that IOH-NPs with gemcitabine triphosphate (GTP) as the drug anion ( $[\text{ZrO}]^{2+}_3[\text{GTP}]^{3-}_2$  IOH-NPs) can be realized similarly, showing comparable properties as  $[\text{ZrO}]^{2+}[\text{GMP}]^{2-}$  IOH-NPs (Table S1 and Figure S7, Supporting Information).

In addition to  $[\text{ZrO}]^{2+}[\text{GMP}]^{2-}$  IOH-NPs as active drug-loaded nanocarrier,  $[\text{ZrO}]^{2+}[\text{CMP}]^{2-}$  IOH-NPs (CMP: cytidine monophosphate) were prepared as GEM-free reference via a similar synthesis protocol (Figures S1–S5, Supporting Information). In difference to GMP, CMP does not contain fluorine in 2,2'-position of the ribose unit, so that the DNA reproduction is not blocked. Beside the cytostatic activity,  $[\text{ZrO}]^{2+}[\text{GMP}]^{2-}$  and  $[\text{ZrO}]^{2+}[\text{CMP}]^{2-}$  IOH-NPs exhibit similar properties (size, composition, etc.) within the significance of the analytical characterization (Figures S1–S6, Supporting Information). Therefore, GEM-free  $[\text{ZrO}]^{2+}[\text{CMP}]^{2-}$  IOH-NPs were used in the following (with similar concentration as  $[\text{ZrO}]^{2+}[\text{GMP}]^{2-}$ ) as negative control without any cytostatic effect. Moreover, solutions of  $\text{H}_2(\text{GMP})$  and free GEM were used (with similar GMP/GEM concentration as in  $[\text{ZrO}]^{2+}[\text{GMP}]^{2-}$ ) as positive control. To avoid lengthy chemical formula,  $[\text{ZrO}]^{2+}[\text{GMP}]^{2-}$  IOH-NPs are designated as GMP-IOH-NPs and  $[\text{ZrO}]^{2+}[\text{CMP}]^{2-}$  IOH-NPs as Ref-IOH-NPs in the discussion of the in vitro/in vivo studies (Figure 1f).

## 2.2. Fluorescence Labeling and Surface Functionalization

To enable  $[\text{ZrO}]^{2+}[\text{GMP}]^{2-}$  IOH-NPs for fluorescence-based tracking in vitro and in vivo, they were labeled with fluorescent dyes showing green (DY-549P1-dUTP, designated DUT549) or red (DY-647P1-dUTP, designated DUT647) emission. Due to their bright emission, only very low amounts ( $\approx 0.01$  mol-%) of the respective dye anions are required, as expressed by a composition such as  $[\text{ZrO}]^{2+}[(\text{GMP})_{>0.99}(\text{DUT647})_{<0.01}]^{2-}$ . Successful incorporation of the fluorescent dye is visualized by the characteristic emission (Figure S6, Supporting Information).

To enhance the tumor uptake of  $[\text{ZrO}]^{2+}[\text{GMP}]^{2-}$  IOH-NPs, we pursued two strategies for surface modification. On the one hand, the IOH-NPs were coated with glucose (GLU), and on the other hand, functionalized with cetuximab (CTX) as pancreatic-tumor-specific antibody. To this concern, we have coated  $[\text{ZrO}]^{2+}[\text{GMP}]^{2-}/[\text{ZrO}]^{2+}[\text{CMP}]^{2-}$  IOH-NPs with a shell of  $[\text{ZrO}]^{2+}[\text{G6P}]^{2-}$  (G6P: glucose-6-phosphate) as another type of IOH-NPs (Table S2 and Figures S8–S10, Supporting Information). The course of the coating can be followed by the zeta potential (Figure 1e). For CTX functionalization, an aqueous CTX solution was slowly added to a suspension of  $[\text{ZrO}]^{2+}[\text{GMP}]^{2-}/[\text{ZrO}]^{2+}[\text{CMP}]^{2-}$  IOH-NPs, whereupon the antibody was electrostatically adsorbed on the particle surface. Successful adhesion of CTX was qualitatively indicated by an increased particle diameter ( $84 \pm 19$  nm) as well as by a zeta potential, which decreases after CTX functionalization ( $-21 \pm 7$  mV) in comparison to non-CTX-functionalized IOH-NPs ( $-35 \pm 6$  mV, Figure 1e,f; Tables S3–S5 and Figures S11–S15, Supporting Information). The decreased surface charge is in accordance with the alkaline point of zero charge for CTX ( $\text{PZC}_{\text{CTX}}$  at pH = 8.5).<sup>[20]</sup> The amount of CTX adhered on the particle surface was adjusted and determined by Bradford assays (Table S5 and Figure S14, Supporting Information) and resulted in  $0.2 \text{ mg mL}^{-1}$  CTX for  $[\text{ZrO}]^{2+}[\text{GMP}]^{2-}$ @CTX suspensions with a particle content of  $1 \text{ mg mL}^{-1}$ , so that these IOH-NPs contain 63% GMP of the total IOH-NP mass. Finally, immunofluorescence assays confirm CTX to selectively bind to hEGFR1 after adhesion on the IOH-NP surface (Figure S15, Supporting Information). In in vitro/in vivo studies, the GLU-coated/CTX-functionalized nanocarriers are designated GMP-GLU-IOH-NPs and GMP-CTX-IOH-NPs (Figure 1f).

## 3. In Vitro Characterization

### 3.1. Cell Uptake

Efficient uptake by tumor cells, followed by efficient drug release is crucial for the efficacy of nanocarriers, in general.<sup>[18,19]</sup> To this concern, the uptake of DUT549-labeled Ref-IOH-NPs was investigated first of all in two PDAC cell lines: i) AsPC1—a human cell line known to moderately to strongly express human EGFR1, recognized by the recombinant antibody CTX (Figure S16, Supporting Information) and ii) Panc02—a murine cell line that by definition lacks the human EGFR epitope.<sup>[21]</sup> To avoid any drug-mediated toxicity (possibly affecting cell proliferation, morphology, adhesion, etc.), GEM-free Ref-IOH-NPs were applied as such or after GLU coating or CTX functionalization (Ref-GLU-IOH-NPs, Ref-CTX-IOH-NPs). Both cell types show efficient massive

uptake of all tested IOH-NPs within 48 h (Figure 2a,b). In AsPC1 cells, the IOH-NP uptake was even faster (already after 30 min) and slightly higher (Figure 2a) than in Panc02 cells (after  $\approx 5$  h) (Figure 2b). Interestingly, neither GLU coating nor CTX functionalization of the IOH-NPs increased their cellular uptake in the in vitro monolayer setting. By assessing the intracellular trafficking in AsPC1 cells, DUT647-labeled GEM-free Ref-IOH-NPs turned out to end up in part in LysoTracker-positive late endosomes and lysosomes (Figure 2c). Thus, the IOH-NPs can be assumed to follow the endocytic pathways for cell internalization, before they reach these acidic compartments. Such mechanism is known for a variety of nanocarriers<sup>[14]</sup> and also in accordance with our previous findings, showing IOH-NPs to end up in late endosomes (large endosomal vacuoles) of macrophages 24 h after internalization.<sup>[22]</sup>

As a next step, surface binding of CTX-functionalized IOH-NPs to hEGFR1-expressing AsPC1 cells was analyzed. Binding experiments were performed by incubating cells with Ref-CTX-IOH-NPs at 4 °C (Figure S16, Supporting Information). At this temperature, the cellular metabolism and internalization processes are minimalized. As expected, almost no cell uptake occurred at 4 °C, neither by AsPC1 nor by Panc02 cells. Notably, Ref-CTX-IOH-NPs were nevertheless observed via confocal fluorescence microscopy only on the cell surface of AsPC1 cells but not on hEGFR1 non-expressing murine Panc02 cells, which confirms receptor-mediated binding of Ref-CTX-IOH-NPs to the hEGFR1 epitope. The ability of DUT549-labeled IOH-NPs to be efficiently taken up by PDAC cells shows their potential to serve as nanocarriers for image-guided delivery of GEM to tumor tissue.

Aiming at an in vitro evaluation of the cytotoxic effects, AsPC1 and Panc02 cells were incubated with increasing concentrations of the DUT549-labeled GMP-IOH-NPs and GTP-IOH-NPs, as well as with GLU-coated and CTX-functionalized IOH-NPs (Figure 2d,e). Note that GTP-IOH-NPs with gemcitabine triphosphate were studied here, too. The efficacy of the IOH-NPs was compared to Ref-IOH-NPs (negative control) and free GEM (positive control). In all experiments, the specified GMP/GTP/GEM concentration refers to the respective concentration in the IOH-NPs. Cell growth was monitored with a live-cell imaging system. The concentration-dependent efficacy was measured as a percentage of the cell confluence after 72 h of incubation—a point in time when the control cells already reached full confluence. As a result, AsPC1 cells show a concentration-dependent sensitivity to GMP-IOH-NPs/GTP-IOH-NPs with a half-maximal inhibitory concentration ( $\text{IC}_{50}$ ) of 14.8 nM in comparison to an  $\text{IC}_{50}$  of 10.5 nM of free GEM. Both values are even lower than the  $\text{IC}_{50}$  of the GEM values described in the literature at 72 h ( $494 \text{ nM}$  to  $23.9 \text{ }\mu\text{M}$ ).<sup>[23]</sup> In this regard, human PDAC cell lines are known in particular for a varying sensitivity to GEM, mainly driven by different expression of its molecular regulators.<sup>[24]</sup> A therapeutic approach that allows circumventing the cell-intrinsic GEM processing and the GEM cell-transport mechanisms responsible for chemoresistance, therefore, can become even more interesting, especially in regard of the genomic heterogeneity of PDAC, as well as the intrinsic and developed chemoresistance to GEM, which severely limit its effectiveness.

GMP-IOH-NPs and GTP-IOH-NPs generally show a lower sensitivity in Panc02 cells than in AsPC1 cells (Figure 2d,e),

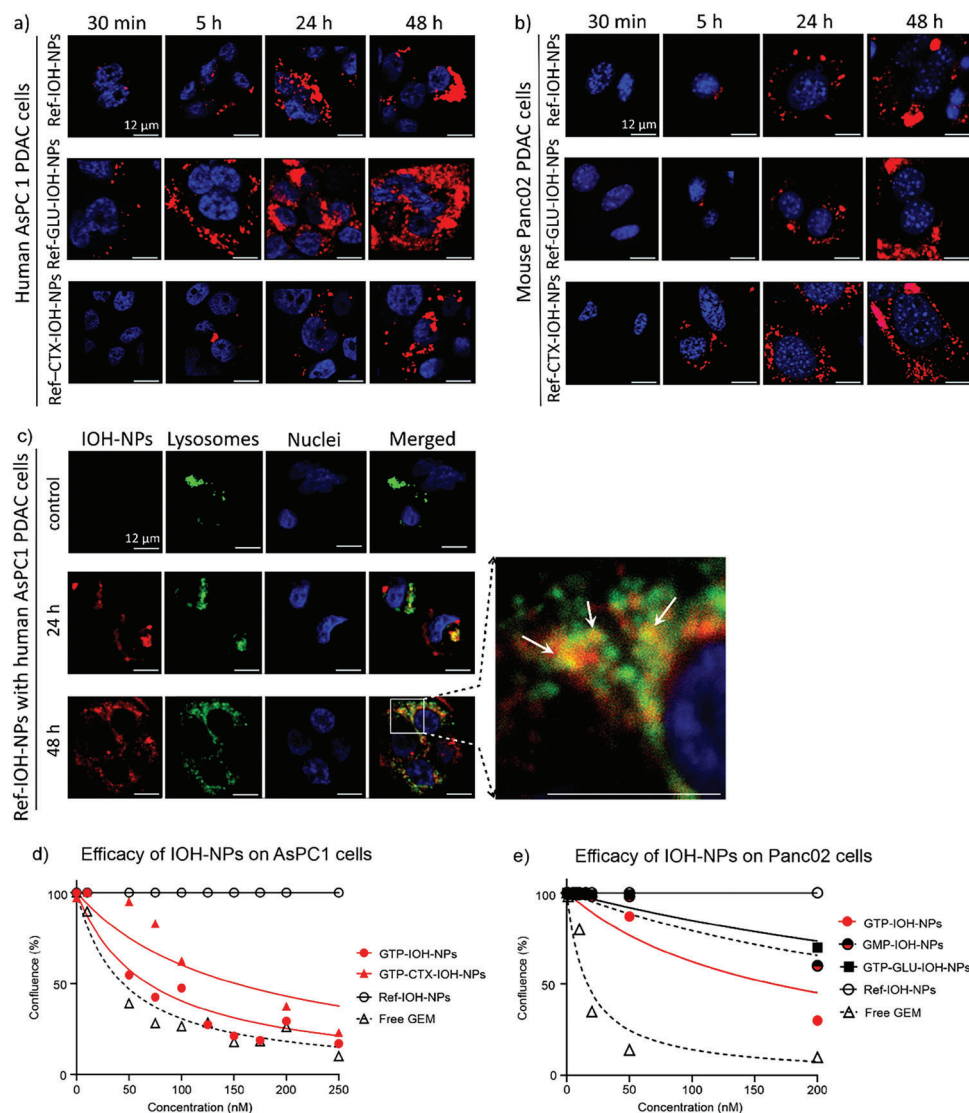


**Figure 2.** In vitro uptake and antiproliferative efficacy of IOH-NPs on PDAC cells. a,b) Representative confocal fluorescence microscopy images showing time-dependent uptake of DUT549-labeled Ref-IOH-NPs, Ref-GLU-IOH-NPs (glucose-coated), Ref-CTX-IOH-NPs (CTX-functionalized) by human AsPC1 (a) and murine Panc02 cells (b) (red: DUT549-labeled IOH-NPs,  $\lambda_{Ex} = 561$  nm,  $\lambda_{Em} = 571$ –623 nm; blue: nuclei stained with DAPI,  $\lambda_{Ex} = 405$  nm,  $\lambda_{Em} = 415$ –479 nm). c) Representative confocal fluorescence microscopy images showing the uptake of DUT647-labeled Ref-IOH-NPs (red;  $\lambda_{Exc} = 647$  nm,  $\lambda_{Em} = 643$ –750 nm) after 24 and 48 h in AsPC1 cells co-stained with LysoTracker (green: acidic compartments of cells, mainly lysosomes, together with late endosomes and multivesicular bodies;  $\lambda_{Ex} = 594$  nm,  $\lambda_{Em} = 577$ –594 nm; blue: nuclei stained with DAPI). The enlarged section shows GEM-free Ref-IOH-NPs to colocalize in part with LysoTracker-labeled vesicles (yellow, marked with white arrows on inset). Note that more LysoTracker-labeled vesicles are visible in comparison to the control without IOH-NPs (scale bars in a–c identical for all images). d,e) Response of PDAC cells to treatment with GMP-IOH-NPs and GTP-IOH-NPs (GMP: gemcitabine monophosphate, GTP: gemcitabine triphosphate) as well as the respective GLU-coated and CTX-functionalized GMP/GTP-IOH-NPs by human AsPC1 (d) and murine Panc02 cells (e) assessed 72 h after treatment with annotated IOH-NPs or free GEM.

whereas the anti-proliferative effect of free GEM on Panc02 cells ( $IC_{50}$ : 15.9 nM) is comparable to that on AsPC1 cells ( $IC_{50}$ : 10.5 nM). GTP-IOH-NPs were even  $\approx 10$ -times less cytotoxic in Panc02 cells ( $IC_{50}$ : 149.2 nM) than in AsPC1 cells ( $IC_{50}$ : 14.8 nM) (Figure 2d,e), which can be ascribed to the generally slower uptake of IOH-NPs into Panc02 cells than into AsPC1 cells (Figure 2a,b). Furthermore, GTP-IOH-NPs ( $IC_{50}$ : 149.2 nM)—containing the phosphorylated and pharmacological active form of GEM—were more effective in Panc02 cells

than GMP-IOH-NPs ( $IC_{50}$ : 459 nM) (Figure 2e). This finding can be ascribed to the fact that GTP does not need any further phosphorylation within the cells to be incorporated into the DNA. In addition, GTP is not transported out of the cell (in difference to GMP), since this triphosphorylated GEM metabolite is protected against deamination and cell efflux.<sup>[8]</sup> Since the formation of GMP is the rate-limiting step for the whole phosphorylation process to activate pharmacological GEM within the cell—with downregulation of the responsible enzyme dCK

being an essential reason for drug resistance, IOH-NP-driven direct delivery of GMP into cells can be of course highly promising to overcome GEM chemoresistance. As GTP-IOH-NPs can be prepared similarly (Table S1 and Figure S7, Supporting Information), furthermore, a direct delivery of GTP to tumor sites via IOH-NPs as drug-delivery system is also possible.

Interestingly, the therapeutic efficacy was not improved when using CTX-functionalized IOH-NPs, showing a two-times lower efficacy ( $IC_{50}$ : 38.4 nM) than non-functionalized IOH-NPs (Figure 2d). Similarly, glucose-coated IOH-NPs did not improve the anti-proliferative potential. In contrast, Panc02 cells were even  $\approx 25$ -times less responsive to GTP-GLU-IOH-NPs than to free GEM as the clinical counterpart. They were even less effective than non-coated GMP-IOH-NPs/GTP-IOH-NPs (Figure 2e). Hence, “naked” GMP-IOH-NPs/GTP-IOH-NPs—at least in cell-based assays—show the best performance for GEM delivery. Both GLU-coated and CTX-functionalized IOH-NPs nevertheless remain promising tools for targeted delivery in vivo.

### 3.2. hENT1 Inhibition to Overcome Chemoresistance

A major drawback of GEM therapy relates to the development of chemoresistance, which very often occurs during the course of treatment, e.g. due to altered expression of the hENT1 transporter, responsible for GEM cellular uptake.<sup>[25]</sup> To this concern, a hENT1-independent uptake of IOH-NPs can be an ideal option to overcome one of the underlying mechanisms of chemoresistance. Therefore, we have first analyzed if the inhibition of the hENT1 with the selective tyrosine kinase inhibitor nilotinib could affect the internalization of the different GMP-IOH-NPs.<sup>[26]</sup> AsPC1 cells expressing hENT1 were seeded on coverslips and incubated for 24 h with 10  $\mu\text{M}$  nilotinib (see Supporting Information). Then, GMP-IOH-NPs, GMP-CTX-IOH-NPs, Ref-IOH-NPs and free GEM were added with a concentration of 37.5 ng mL<sup>-1</sup>. The cellular uptake was assessed after 30 min, 5, 24 and 48 h with confocal fluorescence microscopy. As a result, AsPC1 cells indeed show efficient IOH-NP uptake, even during hENT1 inhibition with nilotinib (Figure 3a) and with uptake rates comparable to cells with active hENT1 transporter (Figure 2a). This clearly proves the uptake of GMP-IOH-NPs to be independent of the activity of the hENT1 transporter.

As a second step, we have investigated if hENT1 inhibition has an impact on the efficacy of GEM-IOH-NPs. To this concern, AsPC1 cells were pre-incubated for 24 h with 10  $\mu\text{M}$  of nilotinib and treated with IOH-NPs in a concentration of 300 nM. The cell viability was assessed after 24, 48, and 72 h using a CellTiter-Glo assay (see Supporting Information). As a result, free GEM efficiently reduces the cell viability only in absence of nilotinib (Figure 3b). Its cytotoxic effect was almost completely abolished by inhibiting hENT1, indicating that GEM was not transported into the cells in the presence of nilotinib. In contrast, the efficacy of both GMP-IOH-NPs and GMP-CTX-IOH-NPs was not or only slightly affected by nilotinib, which suggests an uptake of the IOH-NPs via a different mechanism. Moreover, hENT1 ex-

pression was observed in all AsPC1 tumors, independent of their treatment with GMP-IOH-NPs or free GEM as shown by immunohistochemical staining (see Supporting Information). The fact that the nanoparticle uptake is independent from hENT1 enables GMP-IOH-NPs to establish high GMP concentrations in cells—even in absence of hENT1—and to nevertheless develop their full antitumoral effect. This indicates the IOH-NPs to be able to overcome endosomal entrapment and to efficiently release GMP into the cytosol, which then leads to an inhibition of the DNA synthesis. Since the tumor level of hENT1 is known to be prognostic in PDAC patients treated with adjuvant GEM chemotherapy,<sup>[27]</sup> bypassing the hENT1 transporter with high-load GMP-IOH-NPs has the potential to overcome intrinsic and acquired hENT1-mediated GEM resistance. Such strategy was already suggested<sup>[13]</sup> but is yet limited to nanocarriers with complex composition and low GEM load (<10% of total nanocarrier weight).

In addition to by-passing the hENT1 transporter, GMP-IOH-NP-driven delivery to the site of the tumor could also allow an intracellular GEM activation independent of dCK. The important role of dCK in mechanisms causing chemoresistance was shown with several human PDAC cell lines and in PDAC patients, in which the expression level of dCK was found to correlate with the degree of GEM resistance. Thus, knockdown of dCK results in GEM resistance, whereas an overexpression of dCK in GEM-resistant cell lines restores the sensitivity to GEM treatment.<sup>[9a]</sup> The administration of free GEM, however, is hampered by its poor stability in biological media and its poor cellular uptake.<sup>[28]</sup> The use of GMP-IOH-NPs to deliver already phosphorylated GMP to tumor cells, thus, has the additional advantage not only to be independent of hENT1 for cellular uptake but also of the enzyme dCK for GEM activation. Both is extremely important to overcome GEM chemoresistance and to establish an efficient treatment for PDAC patients, which is even suitable for long periods of administration.

## 4. In Vivo Studies

### 4.1. Biodistribution

Prior to in vivo efficacy studies, the biodistribution of the different IOH-NPs was assessed, in general, depending on the application route in either immunodeficient xenogenic (AsPC1) or immunocompetent syngeneic (Panc02) orthotopic PDAC mouse models (Figures 4-; Figures S17–S29, Supporting Information). Fluorescence imaging (FI) was applied taking advantage of DUT647-labeled IOH-NPs. Similar to the in vitro studies, Ref-IOH-NPs7 were used as GEM-free reference (negative control). Mice bearing orthotopic AsPC1 tumors (Figure S17, Supporting Information) were injected either intraperitoneally (i.p.) or intravenously (i.v.) with a single dose of Ref-IOH-NPs, Ref-CTX-IOH-NPs or Ref-GLU-IOH-NPs (all DUT647-labeled) in low concentrations, corresponding to 3.5 mg kg<sup>-1</sup> body weight (BW) of cytidine monophosphate.

Mice were sacrificed 48 h after injection and the fluorescence intensity of the different IOH-NPs measured ex vivo by FI to assess their biodistribution, accumulation in tumors and in distant tumor lesions, as well as in excretion organs (kidneys, liver).

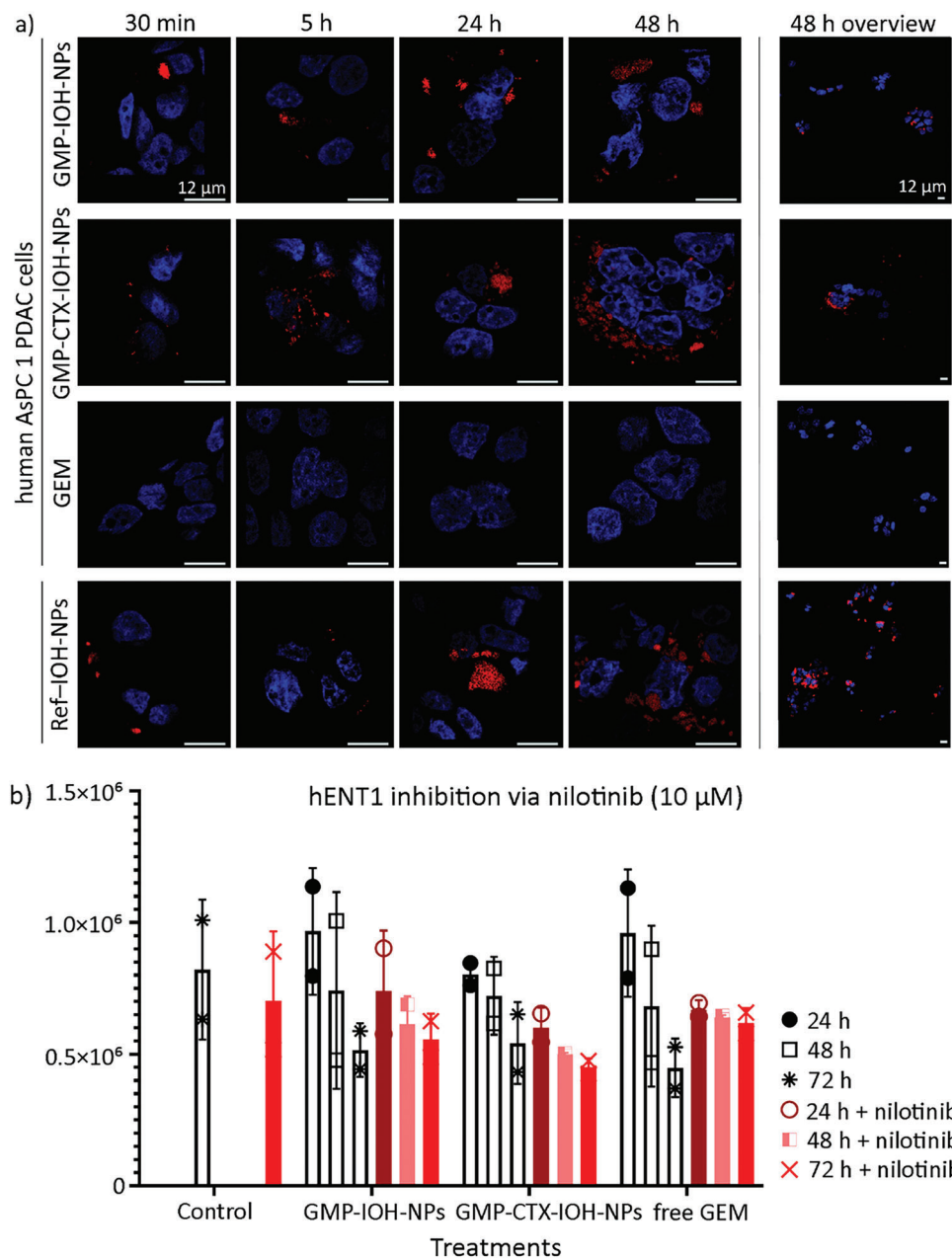


**Figure 3.** Efficacy of GMP-IOH-NPs and relation to hENT1. a) Uptake of DUT647-labeled GMP-IOH-NPs, GMP-CTX-IOH-NPs and Ref-IOH-NPs ( $37.5 \text{ ng mL}^{-1}$ ) upon pre-incubation of AsPC1 cells with  $10 \mu\text{M}$  nilotinib (red: IOH-NPs,  $\lambda_{\text{Exc}} = 647 \text{ nm}$ ,  $\lambda_{\text{Em}} = 643\text{--}750 \text{ nm}$ ; blue: nuclei stained with DAPI,  $\lambda_{\text{Exc}} = 405 \text{ nm}$ ,  $\lambda_{\text{Em}} = 415\text{--}479 \text{ nm}$ ). Images on right side show an overview after 48 h of incubation (lower magnification). b) Efficacy of GMP-IOH-NPs, GMP-CTX-IOH-NPs and free GEM (concentration each:  $300 \text{ nM}$ ) on AsPC1 cells upon 24 h pretreatment with (pink-red bars, squares) and without (white-gray bars, circles) nilotinib ( $10 \mu\text{M}$ ). Cell viability assessed after 24, 48, and 72 h using luminescent CellTiter-Glo assay.

The fluorescence of the IOH-NPs was clearly detectable with ex vivo scans of organs/tumors and metastasis, showing high IOH-NP accumulation after 48 h at the tumor sites. This already proves their great potential for tumor-selective drug delivery (Figure 4a,b: upper panels). All IOH-NPs show efficient tumor uptake with slightly higher tumor accumulation after i.p. administration (Figure S18, Supporting Information). Light sheet fluorescence microscopy (LSFM) reveals an inhomogeneous 3D distribution of the IOH-NPs in excised and cleared tumors. Spe-

cific fluorescence signals were detected mostly in the periphery of the tumors due to the restricted tissue penetration of the IOH-NPs (Figure 4a,b: middle panels).<sup>[15]</sup> Moreover, IOH-NPs frequently form clusters within the 3D architecture of the tumor tissue, leading to remarkably intense fluorescence signals. This was observed to be independent from the application route and for all types of Ref-IOH-NPs, especially for Ref-GLU-IOH-NPs. Taken together, multiscale FI demonstrates that the IOH-NPs are effectively delivered in mice to the tumor site, as well as to

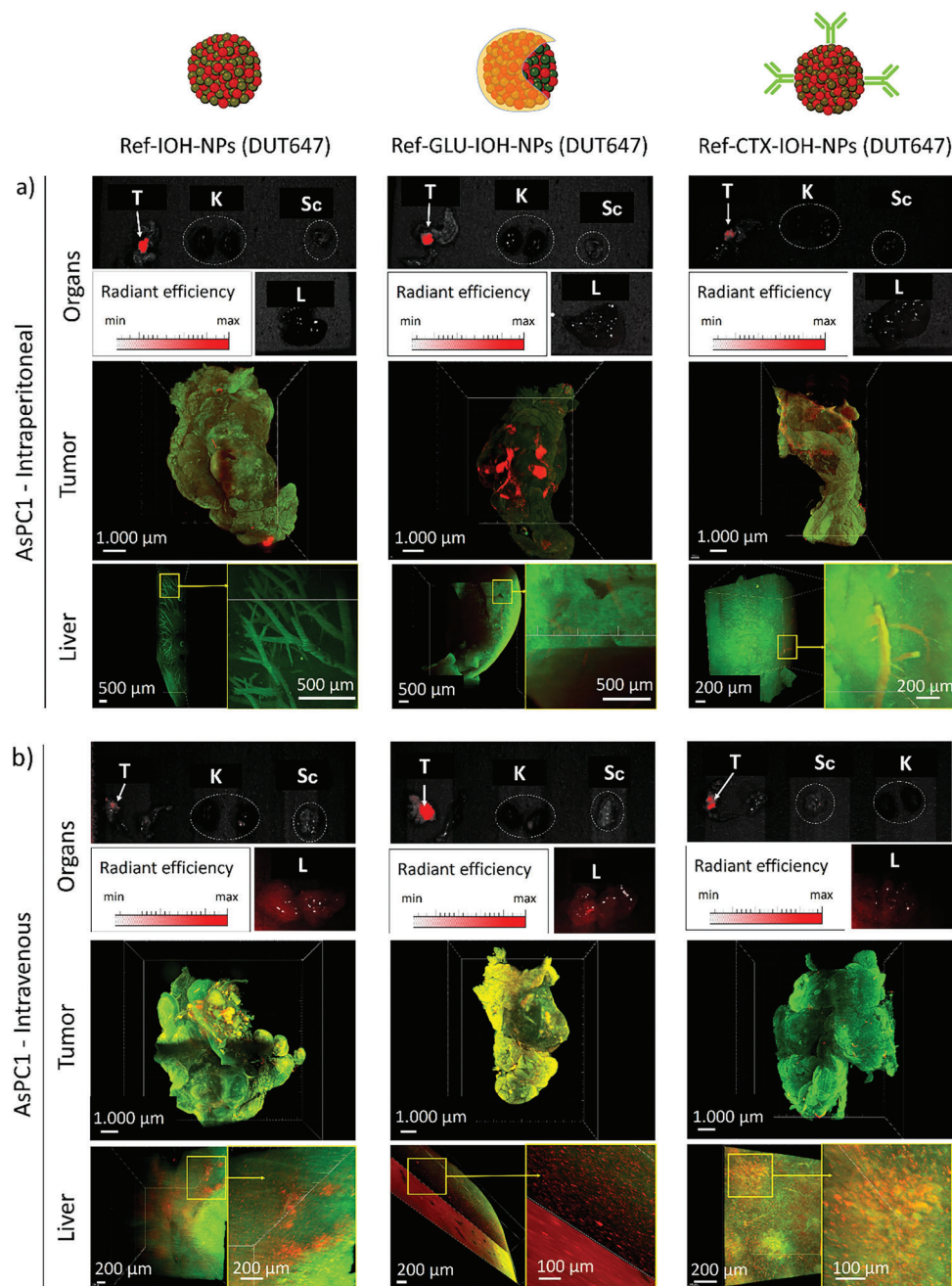


**Figure 4.** Biodistribution of IOH-NPs in AsPC1 tumors and organs depending on application route and type of DUT647-labeled IOH-NPs: Ref-IOH-NPs (left), Ref-GLU-IOH-NPs (middle), Ref-CTX-IOH-NPs (right) applied i.p. (a) or i.v. (b) as single bolus (48 h before dissection/scanning, containing equivalent of cytidine monophosphate to 3.5 mg GEM/kg BW). The upper panels show ex vivo FI scans of excised organs/tissues: tumor (T), scar after surgical intervention (Sc), both kidneys (K), liver (L). Middle-/lower panels show representative LSFM images of tumor and pieces of liver tissue ( $\approx 1 \text{ cm}^3$ ) illustrating IOH-NP distribution (red: IOH-NPs,  $\lambda_{\text{Ex}} = 630/30 \text{ nm}$ ,  $\lambda_{\text{Em}} = 680/30 \text{ nm}$ ; green: tissue autofluorescence,  $\lambda_{\text{Ex}} = 520/40 \text{ nm}$ ,  $\lambda_{\text{Em}} = 585/40 \text{ nm}$ ). Clustered distribution pattern of IOH-NPs within tumors, mainly for Ref-GLU-IOH-NPs and high accumulation of all tested IOH-NPs within liver only after i.v. injection (yellow boxes on liver scans indicate areas displayed also with high magnification).

metastatic sites, and predominately to the tumor periphery. In this way, the growth of the tumor can be limited and efficiently reduced with IOH-NPs serving as a drug reservoir at the border of the tumor.

Interestingly, the route of application significantly affects the accumulation of IOH-NPs in the liver. Thus, no IOH-

NP-derived fluorescence was observed after i.p. administration (Figure 4a), whereas liver accumulation occurred with i.v. application (Figure 4b). This was also reported by others, e.g., after i.v. application of gemcitabine-loaded PEGylated liposomes.<sup>[29]</sup> The highest fluorescence signal over the liver was detected with non-functionalized Ref-IOH-NPs, followed by

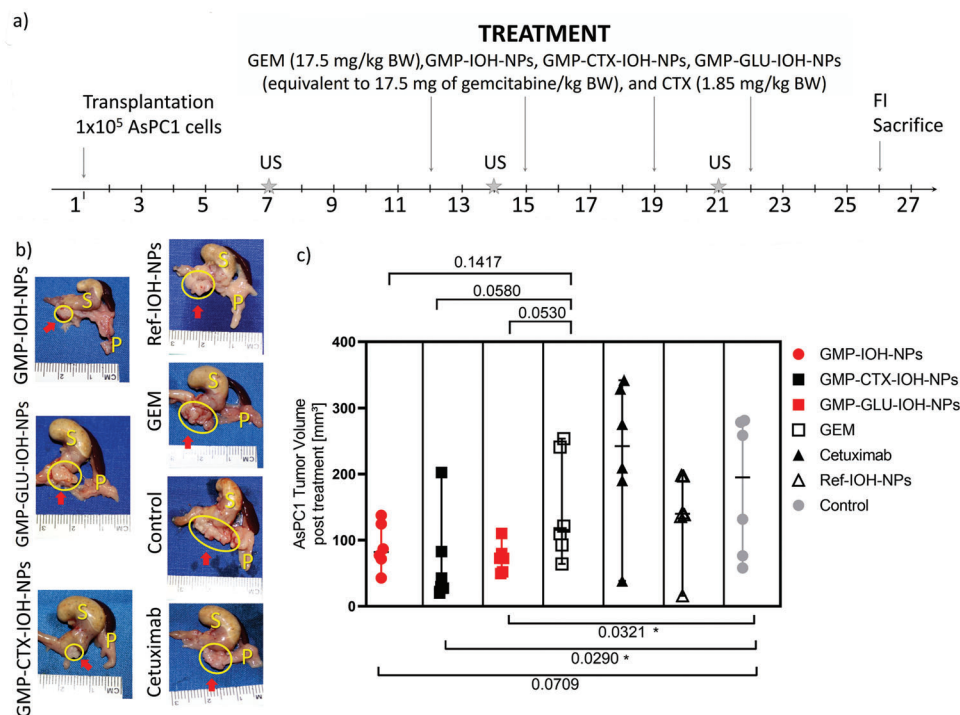


**Figure 5.** In vivo antitumor efficacy of IOH-NPs in AsPC1 tumor bearing mice. a) Treatment scheme (US: ultrasonography, FI: fluorescence imaging). b) Representative images of tumors (yellow circles, red arrows) adjacent to stomach (S) and pancreas (P) during autopsy. c) Tumor volumes assessed during autopsy by caliper measurement. Graph shows tumor size in response to therapy at the time of dissection, together with median and range ( $p \leq 0.05$ ; \*marked considered statistically significant;  $n = 6$ ) (see Figure S19 for body weight and blood parameters).

Ref-Glu-IOH-NPs, whereas Ref-CTX-IOH-NPs exhibit the lowest liver uptake ( $\approx 2.5$ -times lower fluorescence signal; Figure 4b: upper panels; Figure S18, Supporting Information). For all IOH-NPs, the average fluorescence signal over the liver (ex vivo 48 h after i.v. application) was comparable to the signal over the tumors (Figure S18, Supporting Information). LSFM of pieces of liver tissue ( $\approx 1 \text{ cm}^3$ ) show intrahepatic IOH-NPs to be homogeneously distributed and only with minor clusters (Figure 4b: lower panels). This agrees with the previously described high uptake of i.v.-injected nanocarriers by liver-resident macrophages (Kupfer cells),<sup>[30]</sup> which are key-players in the hepatic sequestration of nanocarriers or nanocarrier elimination via the hepatobiliary excretory pathway. Beside the liver, none of the IOH-NPs and administration routes resulted in a detectable fluorescence signal ex vivo over kidneys (Figure 4a,b: upper panels) or spleen (data not shown), where splenic macrophages also play a significant role for the removal of nanocarriers from blood. Here, the accumulation in cells of the reticuloendothelial system (RES as heterogeneous population of phagocytic cells) has been described to significantly capture nanocarriers and to reduce nanocarrier half-life, which is a major barrier for the implementation of nanocarriers to clinical use.<sup>[31]</sup>

Despite the already low uptake in kidneys and spleen, the i.p. route—at least in mice—represents the first choice for preclinical therapy-efficacy studies to avoid liver uptake and to further prolong the half-live time of the IOH-NPs. This measure is in accordance with other studies showing subcutaneous (s.c.) and i.p. injection to result in lower nanocarrier accumulation in the liver than the i.v. route.<sup>[32]</sup> Ensuring optimal clearance conditions to-

gether with best drug delivery to the target region, in this regard, requires suitable nanocarriers, as well as the most effective route of administration.

#### 4.2. Treatment Efficacy and GMP Delivery Assessment

Since i.p. application resulted in the most tumor-selective accumulation of IOH-NPs in PDAC-bearing mice with almost no accumulation within the liver, this route was selected to evaluate the therapeutic efficacy of GMP-IOH-NPs. Although the in vivo studies are focused on GMP-IOH-NPs, it should be noticed that GTP-IOH-NPs can be used as well (Figure S7, Supporting Information). AsPC1- (Figures 5 and 6; Figures S21 and S23, Supporting Information) and Panc02-tumor bearing mice (Figures S20, S22, and S23, Supporting Information) were treated either with GMP-IOH-NPs (all with equivalent to 17.5 mg GEM/kg BW) or free GEM (Gemcitabine Hexal, 17.5 mg GEM/kg BW, positive control) and the corresponding volumes of the negative controls (Ref-IOH-NPs, saline). To analyze if glucose coating affects the treatment efficacy, mice were treated with GMP-GLU-IOH-NPs (equivalent to 17.5 mg GEM/kg BW). To monitor the efficacy of the CTX functionalization in vivo, hEGFR1-expressing AsPC1-tumor-bearing mice were treated with GMP-CTX-IOH-NPs (equivalent to 17.5 mg GEM/kg BW) or the control antibody (1.85 mg CTX/kg BW for each; corresponding to CTX amount on the IOH-NP surface) (Figures 5 and 6). Due to different tumor growth kinetics, treatment started on day 12 for AsPC1 and on day 7 for Panc02 tumor bearing mice.

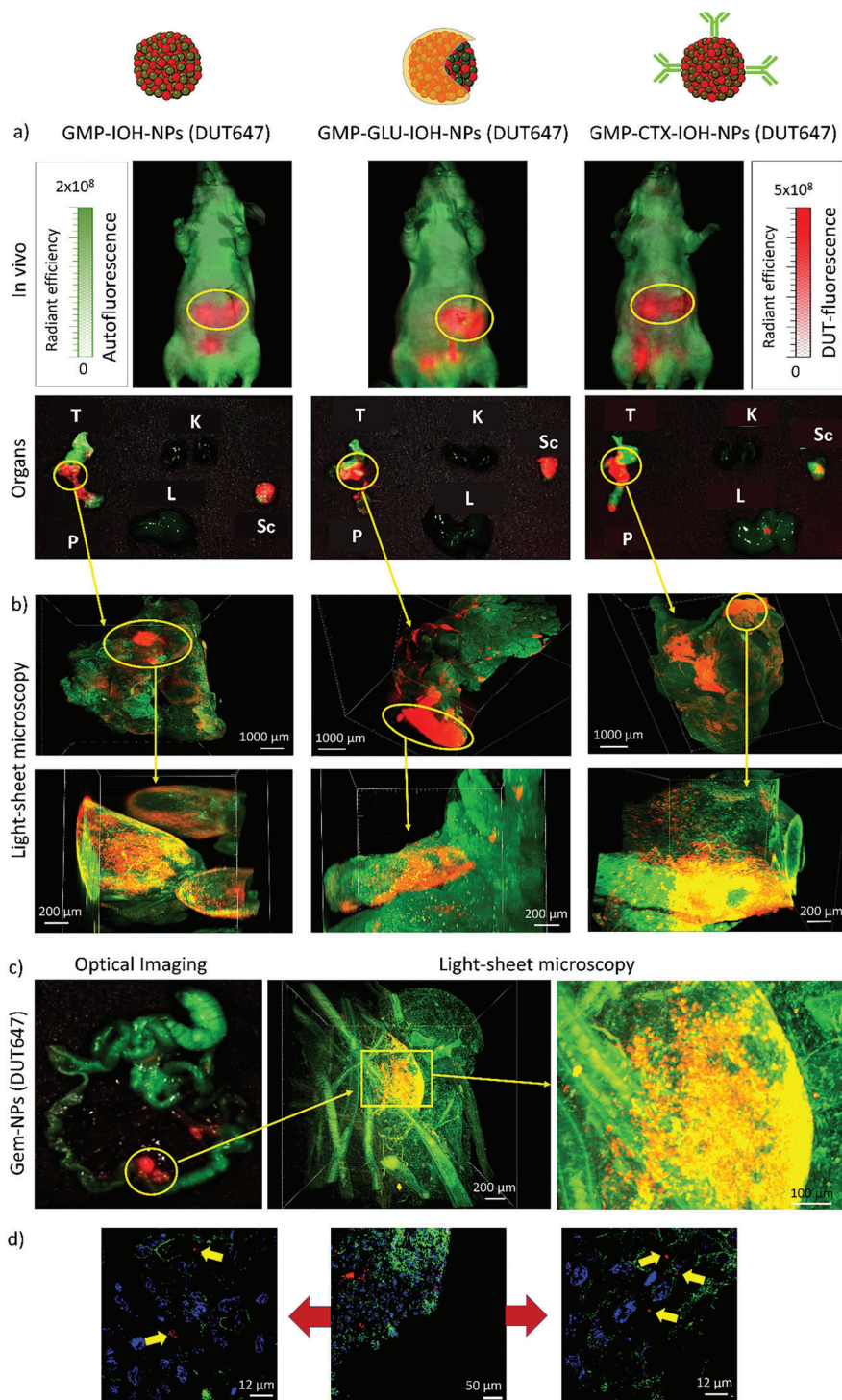


**Figure 6.** Monitoring IOH-NP delivery upon treatment of AsPC1 tumor-bearing mice with DUT647-labeled GMP-IOH-NPs (left), GMP-GLU-IOH-NPs (middle), GMP-CTX-IOH-NPs (right): a) FI (4 days after last treatment; for treatment schedule see: Figure 5a). Spectral unmixing performed to distinguish between DUT647-derived fluorescence (red) and tissue autofluorescence (green). The upper panels show in vivo scans of AsPC1-tumor-bearing mice. The yellow circles label areas where primary tumors develop. The lower panels show ex vivo FI of excised organs shortly after the in vivo scan (T: tumor, P: pancreas, Sc: tumor mass at the scar, K: kidney, L: liver; for GMP-CTX-IOH-NPs fluorescence signal also at site of gallbladder). b) LSFM of cleared tumor tissues (red: DUT647-derived fluorescence,  $\lambda_{\text{Ex}} = 630/30$  nm,  $\lambda_{\text{Em}} = 680/30$  nm; green: tissue autofluorescence,  $\lambda_{\text{Ex}} = 520/40$  nm,  $\lambda_{\text{Em}} = 585/40$  nm). Lower panels with zoomed images of areas labeled by yellow circles (clustered IOH-NP distribution and increased autofluorescence at marginal areas). c) Accumulation of GMP-IOH-NPs (red) in metastatic lesions developed at mesenterium (fluorescence signals visualized by FI and LSFM). d) Immunohistochemical staining of paraffin tumor sections (4 days after GMP-CTX-IOH-NP treatment) with antibody targeting hEGFR1 expressed on cell membrane of AsPC1 cells (green) (blue: nuclei stained with DAPI, red (at yellow arrows): GMP-CTX-IOH-NPs).

In total, animals received four treatment doses according to the treatment schedule (Figure 5a; Figure S20a, Supporting Information). In all mice ultrasonographic examination confirmed the development of a tumor prior to the start of the therapy. Thereafter, tumor progression in response to therapy was assessed weekly by ultrasound (Figure S17, Supporting Information).

In the AsPC1 mouse model, all types of GMP-IOH-NPs show good antitumor efficacy with reduced tumor volumes ( $\approx 50\%$  compared to saline-treated negative control, Figure 5b,c). The highest and significant efficacy was clearly obtained in response to GMP-CTX-IOH-NPs (mean tumor volume:  $61.8 \pm 71.0 \text{ mm}^3$ ) and GMP-GLU-IOH-NPs ( $72.8 \pm 22.0 \text{ mm}^3$ ). Both show significantly smaller tumor sizes than for the negative and positive controls (saline-treated:  $180.8 \pm 104.1 \text{ mm}^3$ ; CTX-treated:  $230.9 \pm 112.4 \text{ mm}^3$ ; GEM-treated:  $147.2 \pm 80.1 \text{ mm}^3$ ). GMP-IOH-NP-treated tumors ( $90.2 \pm 35.2 \text{ mm}^3$ ) were smaller than for the controls but larger than for GLU-coated and CTX-functionalized IOH-NPs. The antitumor effect of the GMP-IOH-NPs was even more pronounced in the syngeneic Panc02 model (Figure S20b,c, Supporting Information). Here, the difference between the efficacy of the GMP-IOH-NPs ( $67 \pm 53 \text{ mm}^3$ ) was not only statistically significant in comparison to the negative control (saline:  $534 \pm 359 \text{ mm}^3$ ), but also in comparison to the positive control (free GEM:  $196 \pm 83 \text{ mm}^3$ ). GMP-IOH-NPs show also a reduced tumor size compared to GMP-GLU-IOH-NPs ( $112 \pm 85 \text{ mm}^3$ ). For Panc02, the average tumor volume of mice treated with Ref-IOH-NPs ( $1055 \pm 931 \text{ mm}^3$ ) was partly larger than of control tumors (saline:  $534 \pm 359 \text{ mm}^3$ ), which, however, was statistically not significant (i.e., two outliers with extremely fast/large grown tumors, resulting in high standard deviations) and could also point to phosphate- and/or cytidine serving as growth factors.<sup>[33]</sup>

In regard of side effects, the general conditions (i.e., BW of mice) were analyzed during the course of therapy, and blood parameters were analyzed after sacrifice. In general, all animals well-tolerated the treatment with IOH-NPs and free GEM without any significant weight loss, signs of deterioration or alteration of hematological and serum parameters (i.e., alanine aminotransferase, blood urea nitrogen, albumin) in the AsPC1 mouse model (Figure S19, Supporting Information). The absence of side effects of free GEM can be explained by a relatively low dose (17.5 mg GEM/kg BW), which is approximately five-times lower as the usually administered GEM dose (100 mg GEM/kg BW). This lower dose was selected in order to be identical to the GMP-load in the IOH-NPs, taking the already strong cytotoxic effect of the GMP-IOH-NPs into account. In vitro hemolysis assays, furthermore, demonstrate a neglectable hemolysis in response to the IOH-NPs (Figure S24, Supporting Information).

In summary, a well-tolerated treatment with GMP-IOH-NPs in PDAC-bearing mice resulted in significantly reduced tumor sizes. Most remarkable, the antitumor effect was even enhanced with GMP-CTX-IOH-NPs, which points to a higher nanoparticle accumulation in the tumor. In comparison to GMP-IOH-NPs, current GEM-based nanocarriers to treat PDAC (e.g., GEM embedded in (bio)polymer matrices or liposomes),<sup>[11,13]</sup> suffer from low drug load (<10% of total nanocarrier mass), multistep synthesis, complex nanocarrier composition and structure, and/or insufficient drug transport, delivery and efficacy.

FI in combination with specific fluorophores is typically hampered by the autofluorescence (e.g., tissue, diet in stomach region). Since each of these sources exhibits specific excitation/emission characteristics, which cannot be exploited if only one-signal emission/excitation filter pairs were utilized, spectral unmixing was applied (see Supporting Information). Multiple measurements (each with different combinations of excitation/emission filters) were performed and the spectral differences of the measured signals used for decoupling, even if detected on the same spot. Applying spectral unmixing, repeated application of DUT647-labeled IOH-NPs to AsPC1 tumor-bearing mice resulted in an intense, specific red fluorescence, which can be detected in whole-body scans over the upper abdomen—the area of pancreatic tumors (Figure 6a; Figure S21a, Supporting Information). This is in contrast to single-dose experiments, where DUT647-labeled IOH-NPs were only detectable *ex vivo* in the excised tumors and organs but hardly detectable *in vivo*. This finding can be attributed to the fact that all mice received a single IOH-NP dose five-times lower (3.5 mg GEM/kg BW) than applied in the efficacy studies (17.5 mg GEM/kg BW). Single-dose addition, however, was repeated in total four-times within two weeks. This proves the IOH-NPs to accumulate in the tumor over time, resulting in a high concentration of DUT647-labeled IOH-NPs serving as a drug reservoir at the tumor site after several treatment cycles. Emission spectra of mice treated with DUT647-labeled GMP-IOH-NPs of cleared AsPC1 tumors show the characteristic red emission within the tumor tissue, which suggests the uptake and presence of the IOH-NPs (Figure S26, Supporting Information). As expected, Ref-IOH-NPs (SI: Figure S21a, Supporting Information) show the same distribution pattern *in vivo* as GEM-IOH-NPs (Figure 6a), proving the good detectability by FI *in vivo* due to the higher IOH-NP concentration after repeated application. Similar results were also obtained in the Panc02 PDAC mouse model (Figure S22, Supporting Information).

In agreement with the biodistribution experiments of Ref-IOH-NPs (Figure 4), GMP-IOH-NPs do not result in any fluorescence signal over the liver after repeated *i.p.* administration—neither in *in vivo* whole-body scans nor in the FI scans of excised organs. The DUT647-derived fluorescence was *in vivo* frequently observed in the area over the bladder (Figure 6a: upper panels; Figure S21a, Supporting Information). In regard of the size limit for renal filtration (6–10 nm),<sup>[34]</sup> the IOH-NPs (hydrodynamic diameter: 60–80 nm) are not expected to be excreted via the renal system. This rather suggests IOH-NP dissolution, followed by renal excretion of the released dye. This is in accordance with the high antitumor efficacy of all GMP-IOH-NPs, which evidences the drug release within the tumor tissue/cells, and thus, also of the fluorescent dye. Moreover, the detection of the DUT647-derived fluorescence signal at the site of the gallbladder suggests the IOH-NPs to be partly excreted by the hepatobiliary system (Figure 6a: lower panel right). The tumor-specific accumulation of the IOH-NPs upon treatment was further confirmed by *ex vivo* scans of the excised organs in the AsPC1 (Figure 6a: lower panels; Figure S21a, Supporting Information) and Panc02 mouse model (Figure S22, Supporting Information). In AsPC1-bearing mice, interestingly, FI revealed a strong accumulation of all IOH-NPs within distant tumor nodules, which frequently develop at the peritoneal scar at

the site of surgical intervention (Figure 6a: labeled with Sc) or within the mesentery (Figure 6c: left). LFSM in 3D proved specific fluorescent signals of DUT647-labeled GMP-IOH-NPs distributed also within mesenteric metastases (Figure 6c: middle, right), which is another most interesting feature of IOH-NPs as tumor-specific nanocarriers. To date, only few studies on PDAC have focused on the enhancement of GEM-loaded nanocarriers at metastatic sites in vivo using imaging (e.g., MRI, NIR-FI),<sup>[35]</sup> although this is a very important information to evaluate the potential of drug delivery systems for PDAC even at late stages.

LSFM of the tumor tissue confirmed IOH-NP accumulation to be associated with a highly-clustered distribution pattern, which was most prominent in GMP-GLU-IOH-NP-treated tumors (Figure 6b). This finding is in accordance with the highest accumulation of IOH-NPs in tumor tissue measured as average fluorescence signal by FI over the tumor area (Figure S23, Supporting Information) and can be associated with high treatment efficacy (Figure 5b,c). Similar to previous results,<sup>[15]</sup> this suggests that also GLU-coating of IOH-NPs can be an effective approach to increase tumor-selective drug delivery and drug protection also in the absence of antibodies and for tumors not targetable with CTX.

Immunofluorescence staining of primary tumors from mice with i.p.-injected GMP-CTX-IOH-NPs, using an anti-human-EGFR antibody, proves the location of DUT647-derived fluorescence signals close to positively stained hEGFR1 tumor cells (Figure 6d). This demonstrates GMP-CTX-IOH-NPs to be valuable tools to monitor the biodistribution, drug delivery, as well as the therapy efficacy, not only to the tumor but also to metastatic lesions on a multiscale level from in vivo over tissue to the cellular level. Moreover, the IOH-NPs accumulate in tumor tissue and ensure a protected delivery of GMP to the tumor site, circumventing chemoresistance and preventing the metabolic inactivation of GEM within the circulation and liver. The good detectability of the IOH-NPs offers an excellent opportunity to understand the pharmacokinetic processes and to further improve the therapeutic options by distinct imaging strategies.

#### 4.3. Intratumoral Toxicity

Tumor sizes, assessed upon different treatment regimens, clearly show a significantly improved efficacy upon treatment with all GMP-IOH-NPs (Figure 5; Figure S21, Supporting Information). Thereof, the best effects were obtained in AsPC1 tumors by GMP-CTX-IOH-NPs. Although the assessment of the tumor sizes is a valuable measure of the chemotherapeutic efficacy per se, other aspects such as the occurrence of necrotic areas or the increase in apoptotic events represent additional aspects of an effective chemotherapy.<sup>[36]</sup> In this regard, necrotic areas were present in AsPC1 tumors after treatment with all IOH-NPs and free GEM (Figure 7). TUNEL assays show a pronounced apoptotic activity, especially in small-sized tumors, excised from mice treated with GMP-CTX-IOH-NPs. Here, the DUT647-derived fluorescence of the IOH-NPs is visible in close proximity to apoptotic cells (Figure 7a,c; Figure S25, Supporting Information). Regions with a high number of apoptotic cells were preferentially lo-

cated at the tumor periphery. This was similarly observed after GMP-GLU-IOH-NP treatment (Figure 7b), which is in agreement with LFSM results, showing them to accumulate in clusters at the tumor margins (Figure 6b). Due to the good tolerability of all GMP-IOH-NPs, their administration beyond the current 2-weeks-period could lead to a further enhancement of the reservoir effect and the antitumor activity. Furthermore, all GMP-IOH-NPs and free GEM (but not Ref-IOH-NPs) result in an infiltration of CD45<sup>+</sup> and CD68<sup>+</sup> immune cells in treated tumors from both AsPC1 (Figure S28, Supporting Information) and Panc02 mouse models (Figure S29, Supporting Information)—a known effect in response to the therapy with free GEM,<sup>[37]</sup> which evidences GMP-IOH-NPs, in addition to the antitumoral effect, to exert similar immune reactions as in response to free GEM.

The high apoptotic activity in tumors in response to GMP-CTX-IOH-NP treatment and the presence of apoptotic cells in close proximity to the IOH-NPs points to a successful delivery of GMP to the tumor sites, an efficient cell uptake and transport into the cytosol for activation, resulting in a high antiproliferative efficacy against PDAC tumors. Preserving the integrity of GMP in the IOH-NPs throughout the delivery process and preventing GMP from degradation in plasma (e.g., by cytidine deaminase/CDA) allows to establish high drug concentrations and a reservoir of IOH-NPs within the tumor with consequent tumor-cell death. Bypassing the primary phosphorylation of GEM by direct delivery of GMP, thus, offers an optimal delivery, especially against GEM-resistant cells.

## 5. Conclusion

Current therapeutic efficacy of GEM suffers from rapid metabolism, high drug dose and drug resistance. To overcome these limitations and to improve the future therapy outcome, we present inorganic–organic hybrid nanoparticles (IOH-NPs) as a novel drug-delivery system. IOH-NPs have a saline composition [ZrO]<sup>2+</sup>[GMP]<sup>2-</sup> (designated GMP-IOH-NPs) and contain GMP as the drug anion with 76% of the total nanoparticle mass. GMP-IOH-NPs exhibit a small, uniform size (29 ± 4 nm), and a high colloidal stability in water (without additional stabilizers or surface functionalization) at high nanoparticle and drug concentration (5 mg mL<sup>-1</sup> IOH-NPs, 3.8 mg mL<sup>-1</sup> GMP). In addition, [ZrO]<sup>2+</sup>[GTP]<sup>2-</sup> IOH-NPs (designated GTP-IOH-NPs) with gemcitabine triphosphate can be also prepared and exhibit similar size, stability and drug load as GMP-IOH-NPs. Efficient uptake of GMP-IOH-NPs is shown into tumor cells in vitro. Fluorescence labeling of the IOH-NP allows to assess their cell-uptake, biodistribution and tumor specific delivery. In this regard, multiscale imaging allows to monitor biodistribution and tumor accumulation from in vivo via tissue to cellular levels by tracking the IOH-NPs, which is an essential key to understand the pharmacokinetic processes and to define an optimal application route.

Multiscale fluorescence microscopy confirms the uptake of the IOH-NPs in tumor cells via endocytosis, followed by intracellular trafficking via endocytic pathways. Although the endosomal escape mechanisms for cytosol delivery of IOH-NPs or already released GMP within endosomal vesicles are not yet sufficiently defined, GMP is finally delivered from the endosomes/lysosomes

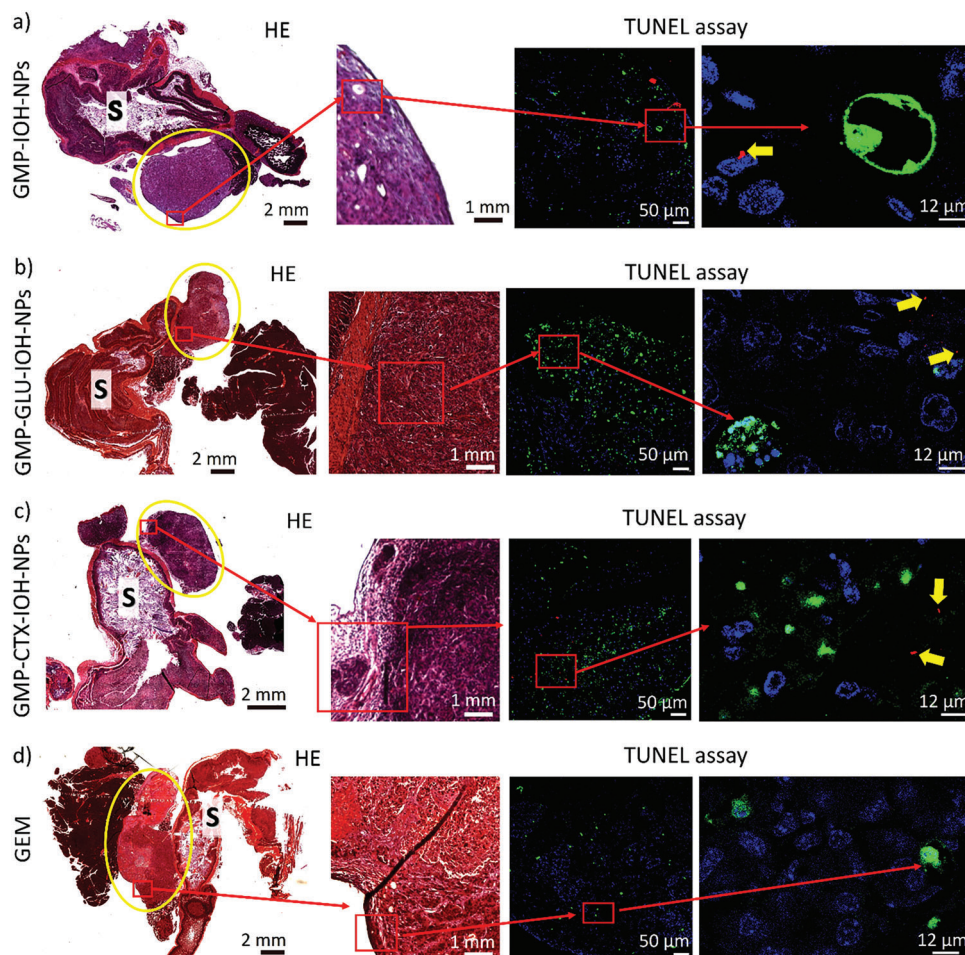


**Figure 7.** Apoptosis detection in AsPC1 tumors after treatment using TUNEL assay. a) GMP-IOH-NPs, b) GMP-GLU-IOH-NPs, c) GMP-CTX-IOH-NPs, d) free GEM (positive control). The left panels show general histology (HE staining) of primary-tumor paraffin sections adjacent to stomach (S) and pancreas (tumors indicated with yellow circles; approximate areas on enlarged images indicated with red squares). The right panels with TUNEL assay analyzed by confocal fluorescent microscopy (green: apoptotic cells; blue: nuclei). The right images represent higher magnifications of areas indicated with red squares. The yellow arrows point to IOH-NPs (red) detectable on the tissue slices in proximity to apoptotic cells.

to the cytosol as demonstrated by their antitumor efficacy. Notably, the uptake of GMP-IOH-NPs is independent of the activity of the human equilibrative nucleoside transporter (hENT1), which is responsible for the transport of free GEM into cells. As a result, IOH-NPs overcome the often occurring chemoresistance of GEM due to a downregulation of hENT1. Most probably, GMP-IOH-NPs are also independent of dCK for GEM activation since the GMP-IOH-NPs already contain phosphorylated GMP. In orthotopic PDAC mouse models, a high accumulation of GMP-IOH-NPs in primary tumor lesions as well as at metastatic sites is verified, which is highly beneficial in treating PDAC since more than half of the patients exhibit metastasis at the time of diagnosis. GMP-IOH-NPs are delivered to tumor cells, protecting GEM during the delivery process by preventing the metabolic inactivation of GEM by enzymes present in the circulation and liver. The treatment with GMP-IOH-NPs is well tolerated and results in a higher antitumor efficacy compared to free GEM, which was enhanced even further applying cetuximab-functionalized GMP-CTX-IOH-NPs.

By minimizing undesired side effects, overcoming chemoresistance, preventing GEM inactivation by delivering already phosphorylated GEM to tumor sites with GMP-IOH-NPs, we could address most of the disadvantages associated with current GEM-based PDAC therapy. Associating the results to therapy efficacy will further support the design of the IOH-NPs as drug-delivery system with a high chance to further improve treatment efficacy. Together with maximizing therapeutic benefits by high drug load, advantageous biodistribution, characterized by almost no liver accumulation but tumor-specific delivery after intraperitoneal application, and the option of long-term GEM treatment by circumventing the mechanisms of chemoresistance, we anticipate GMP-IOH-NPs to have a high chance for improving the quality of life and the survival of PDAC patients.

## Supporting Information

Supporting Information is available from the Wiley Online Library or from the author.

## Acknowledgements

C.F. and J.N. acknowledge the Deutsche Forschungsgemeinschaft (DFG) for funding of the project “Synergistic Image-guided Nanoparticles for Drug Delivery (SIN-Drug)”. Furthermore, K.S., L.S., C.M.N., and C.F. thank the DFG for funding in the Research Training Group (GRK 2039) “Molecular architecture for fluorescent cell imaging”. L.S. and C.M.N. acknowledge financial support through the Helmholtz program “Materials Systems Engineering” under the topic “Adaptive and Bioinspired Materials Systems”. The authors thank Henriette Gröger for excellent assistance regarding chemical synthesis and analytical characterization of IOH-NPs. Furthermore, the authors thank Bärbel Heidrich for excellent assistance in cell culture and together with Sarah Garbode in animal experiments. The authors also thank Regine Kruse, Bettina Jeep, and Sabine Wolfgramm for providing excellent technical assistance for sample preparation, histology and immunohistochemically staining of tissue sections. The authors thank Dr. Christian Dullin for supporting the in vivo optical imaging experiments (spectral unmixing), Dr. Fernanda Ramos for providing protocols for tissue clearing and light sheet microscopy and Dolma Choezom for assisting the proliferation assays. Finally, the authors thank the Light Microscopy Facility of the MPI-NAT for technical support.

Open access funding enabled and organized by Projekt DEAL.

## Conflict of Interest

The authors declare no conflict of interest.

## Data Availability Statement

The data that support the findings of this study are available from the corresponding author upon reasonable request.

## Keywords

chemoresistance, drug delivery, gemcitabine, inorganic–organic hybrid nanoparticles, metastasis, optical imaging, pancreatic cancer

Received: May 30, 2023

Revised: August 15, 2023

Published online:

- [1] R. L. Siegel, K. D. Miller, A. Jemal, *CA Cancer J. Clin.* **2018**, *68*, 7.
- [2] D. Singh, G. Upadhyay, R. K. Srivastava, S. Shankar, *Rev. Cancer* **2015**, *1856*, 13.
- [3] S. Yachida, C. M. White, Y. Naito, Y. Zhong, J. A. Brosnan, A. M. Macgregor-Das, R. Morgan, T. Saunders, D. A. Laheru, J. M. Herman, R. H. Hruban, A. P. Klein, S. Jones, V. Velculescu, C. L. Wolfgang, C. A. Iacobuzio-Donahue, *Clin. Cancer Res.* **2012**, *18*, 6339.
- [4] a) L. D. Wood, M. I. Canto, E. M. Jaffee, D. M. Simeone, *Gastroenterol* **2022**, *163*, 386; b) H. A. Burris 3rd, M. J. Moore, J. Andersen, M. R. Green, M. L. Rothenberg, M. R. Modiano, M. C. Cripps, R. K. Portenoy, A. M. Storniolo, P. Tarassoff, R. Nelson, F. A. Dorr, C. D. Stephens, D. D. Von Hoff, *J. Clin. Oncol.* **1997**, *15*, 2403; c) W. Plunkett, P. Huang, Y. Z. Xu, V. Heinemann, R. Grunewald, V. Gandhi, *Cancer Res.* **1991**, *51*, 6110.
- [5] J. Ciccolini, C. Serdjebi, G. J. Peters, E. Giovannetti, *Cancer Chemother. Pharmacol.* **2016**, *78*, 1.
- [6] D. R. Principe, P. W. Underwood, M. Korc, J. G. Trevino, H. G. Munshi, A. Rana, *Front. Oncol.* **2021**, *11*, 2021.
- [7] D. R. Rauchwerger, P. S. Firby, D. W. Hedley, M. J. Moore, *Cancer Res.* **2000**, *60*, 6075.
- [8] P. Huang, S. Chubb, L. W. Hertel, G. B. Grindey, W. Plunkett, *Cancer Res.* **1991**, *51*, 6110.
- [9] a) Y. Saiki, Y. Yoshino, H. Fujimura, T. Manabe, Y. Kudo, M. Shimada, N. Mano, T. Nakano, Y. Lee, S. Shimizu, S. Oba, S. Fujiwara, H. Shimizu, N. Chen, Z. K. Nezhad, G. Jin, S. Fukushige, M. Sunamura, M. Ishida, F. Motoi, S. Egawa, M. Unno, A. Horii, *Biochem. Biophys. Res. Commun.* **2012**, *421*, 98; b) J. R. Kroep, W. J. Loves, C. L. van der Wilt, E. Alvarez, I. Talianidis, E. Boven, B. J. Braakhuis, C. J. van Groeningen, H. M. Pinedo, G. J. Peters, *Mol. Cancer Ther.* **2002**, *1*, 371.
- [10] a) T. Koltai, S. J. Reshkin, T. M. A. Carvalho, D. Di Molfetta, M. Raffaella Greco, K. O. Alfarouk, R. A. Cardone, *Cancers* **2022**, *14*, 2486; b) Y. Nakano, S. Tanno, K. Koizumi, T. Nishikawa, K. Nakamura, M. Minoguchi, T. Izawa, Y. Mizukami, T. Okumura, Y. Kohgo, *Br. J. Cancer* **2007**, *96*, 457.
- [11] a) Y. Yao, Y. Zhou, L. Liu, Y. Xu, Q. Chen, Y. Wang, S. Wu, Y. Deng, J. Zhang, A. Shao, *Front. Mol. Biosci.* **2020**, *7*, 193; b) G. Mondal, S. Almwash, A. K. Chaudhary, R. I. Mahato, *Mol. Pharm.* **2017**, *14*, 3121; c) T.-J. Liang, Z.-M. Zhou, Y.-Q. Cao, M.-Z. Ma, X.-J. Wang, K. Jing, *Int. J. Pharm.* **2016**, *513*, 564; d) K. K. Frese, A. Neesse, N. Cook, T. E. Bapiro, M. P. Lolkema, D. I. Jodrell, D. A. Tuveson, *Cancer Discovery* **2012**, *2*, 260; e) C. Celia, D. Cosco, D. Paolino, M. Fresta, *Expert Opin. Drug Delivery* **2011**, *8*, 1609.
- [12] a) K. O. Afram, T. Smith, E. Ofori, S. Krishnan, P. Underwood, J. G. Trevino, E. Agyare, *J. Drug Delivery Sci. Technol.* **2020**, *55*, 101374; b) K. Samanta, S. Setua, S. Kumari, M. Jaggi, M. M. Yallapu, S. C. Chauhan, *Pharmaceutics* **2019**, *11*, 574.
- [13] a) A. Patel, A. Saraswat, H. Patel, Z.-S. Chen, K. Patel, *Cancers* **2022**, *15*, 182; b) M. Das, J. Li, M. Bao, L. Huang, *AAPS J.* **2020**, *22*, 88; c) X. Li, G. Salzano, J. Qiu, M. Menard, K. Berg, T. Theodossiou, C. Ladavière, R. Gref, *Front. Bioeng. Biotechnol.* **2020**, *8*, 1027; d) C. Bornmann, R. Graesser, N. Esser, V. Ziroli, P. Jantschkeff, T. Keck, C. Unger, U. T. Hopt, U. Adam, C. Schaechtele, U. Massing, E. von Dobschuetz, *Cancer Chemother. Pharmacol.* **2008**, *61*, 395.
- [14] a) J. J. Rennick, A. P. R. Johnston, R. G. Parton, *Nat. Nanotechnol.* **2021**, *16*, 266; b) S. A. Smith, L. I. Selby, A. P. R. Johnston, G. K. Such, *Bioconjugate Chem.* **2019**, *30*, 263.
- [15] S. A. Torres-Pérez, C. E. Torres-Pérez, M. Pedraza-Escalona, S. M. Pérez-Tapia, E. Ramón-Gallegos, *Front. Oncol.* **2020**, *10*, 605037.
- [16] E. Raymond, S. Faivre, J. P. Armand, *Drugs* **2000**, *60*, 15.
- [17] a) T. Etrych, O. Janoušková, P. Chytil, *Pharmaceutics* **2019**, *11*, 471; b) J. Sophia de Maar, A. M. Sofias, T. P. Siegel, R. J. Vreeken, C. Moonen, C. Bos, R. Deckers, *Theranostics* **2020**, *10*, 1884.
- [18] B. L. Neumeier, M. Khorenko, F. Alves, O. Goldmann, J. Napp, U. Schepers, H. M. Reichardt, C. Feldmann, *ChemNanoMat* **2019**, *5*, 24.
- [19] a) J. Napp, M. A. Markus, J. G. Heck, C. Dullin, W. Möbius, D. Gorpas, C. Feldmann, F. Alves, *Theranostics* **2018**, *8*, 6367; b) M. Poß, E. Zittel, C. Seidl, A. Meschkov, L. Muñoz, U. Schepers, C. Feldmann, *Adv. Funct. Mater.* **2018**, *28*, 1801074; c) J. G. Heck, J. Napp, S. Simonato, J. Möllmer, M. Lange, H. M. Reichardt, R. Staudt, F. Alves, C. Feldmann, *J. Am. Chem. Soc.* **2015**, *137*, 7329.
- [20] Y. Liu, K. Li, B. Liu, S.-S. Feng, *Biomaterials* **2010**, *31*, 9145.
- [21] T. H. Corbett, B. J. Roberts, W. R. Leopold, J. C. Peckham, L. J. Wilkoff, D. P. Griswold Jr, F. M. Schabel Jr, *Cancer Res.* **1984**, *44*, 717.
- [22] a) M. Khorenko, J. Pfeifer, J. Napp, A. Meschkov, F. Alves, U. Schepers, C. Feldmann, *J. Mater. Chem. B* **2023**, *11*, 3635; b) C. Ritschel, J. Napp, F. Alves, C. Feldmann, *Nanoscale* **2022**, *14*, 16249; c) K. Sabljo, J. Napp, F. Alves, C. Feldmann, *Chem. Commun.* **2022**, *58*, 9417.
- [23] N. Awasthi, C. Zhang, A. M. Schwarz, S. Hinz, C. Wang, N. S. Williams, M. A. Schwarz, R. E. Schwarz, *Carcinogenesis* **2013**, *34*, 2361.
- [24] W. Huanwen, L. Zhiyong, S. Xiaohua, R. Xinyu, W. Kai, L. Tonghua, *Mol. Cancer* **2009**, *8*, 125.

- [25] a) Y. Huai, Y. Zhang, X. Xiong, S. Das, R. Bhattacharya, P. Mukherjee, *Cell Stress* **2019**, *3*, 267; b) S. Joseph, B. Word, B. Lyn-Cook, *J. Cancer Res. Ther.* **2018**, *6*, 6.
- [26] V. L. Damaraju, D. Weber, M. Kuzma, C. E. Cass, M. B. Sawyer, *J. Biol. Chem.* **2016**, *291*, 18809.
- [27] J. Spratlin, R. Sangha, D. Glubrecht, L. Dabbagh, J. D. Young, C. Dumontet, C. Cass, R. Lai, J. R. Mackey, *Clin. Cancer Res.* **2004**, *10*, 6956.
- [28] M. Meppen, B. Pacini, R. Bazzo, U. Koch, J. F. Leone, K. A. Koeplinger, M. Rowley, S. Altamura, A. Di Marco, F. Fiore, C. Giuliano, O. Gonzalez-Paz, R. Laufer, V. Pucci, F. Narjes, C. Gardelli, *Eur. J. Med. Chem.* **2009**, *44*, 3765.
- [29] D. Paolino, D. Cosco, L. Racanicchi, E. Trapasso, C. Celia, M. Iannone, E. Puxeddu, G. Costante, S. Filetti, D. Russo, M. Fresta, *J. Controlled Release* **2010**, *144*, 144.
- [30] K. M. Tsoi, S. A. MacParland, X.-Z. Ma, V. N. Spetzler, J. Echeverri, B. Ouyang, S. M. Fadel, E. A. Sykes, N. Goldaracena, J. M. Kathis, J. B. Conneely, B. A. Alman, M. Selzner, M. A. Ostrowski, O. A. Adeyi, A. Zilman, I. D. McGilvray, W. C. W. Chan, *Nat. Mater.* **2016**, *15*, 1212.
- [31] M. Cataldi, C. Vigliotti, T. Mosca, M. Cammarota, D. Capone, *Int. J. Mol. Sci.* **2017**, *18*, 1249.
- [32] L. Harivardhan Reddy, R. K. Sharma, K. Chuttani, A. K. Mishra, R. S. R. Murthy, *J. Controlled Release* **2005**, *105*, 185.
- [33] N. J. Mullen, P. K. Singh, *Nat. Rev. Cancer* **2023**, *23*, 275.
- [34] a) C. F. Adhipandito, S.-H. Cheung, Y.-H. Lin, S.-H. Wu, *Int. J. Mol. Sci.* **2021**, *22*, 11182; b) M. Longmire, P. L. Choyke, H. Kobayashi, *Nanomedicine* **2008**, *3*, 703.
- [35] a) Y. Li, Y. Chen, J. Li, Z. Zhang, C. Huang, G. Lian, K. Yang, S. Chen, Y. Lin, L. Wang, K. Huang, L. Zeng, *Cancer Sci.* **2017**, *108*, 1493; b) S. Matsumoto, K. Nakata, A. Sagara, W. Guan, N. Ikenaga, K. Ohuchida, M. Nakamura, *Oncol. Lett.* **2021**, *22*, 633.
- [36] J. Missbach-Guentner, C. Dullin, S. Kimmina, M. Zientkowska, M. Domeyer-Missbach, C. Malz, E. Grabbe, W. Stühmer, F. Alves, *Neoplasia* **2008**, *10*, 663.
- [37] A. Bulle, J. Dekervel, L. Deschuttere, D. Nittner, L. Libbrecht, R. Janky, S. Plaisance, B. Topal, A. Coosemans, D. Lambrechts, E. Van Cutsem, C. Verslype, J. van Pelt, *Transl. Oncol.* **2020**, *13*, 100743.